NANO LETTERS

pubs.acs.org/NanoLett Letter

Giant Third-Harmonic Optical Generation from Topological Insulator Heterostructures

Yinxiao Xiang, Chenhui Yan, Tudor D. Stanescu, Yanjun Ma, Rishmali Sooriyagoda, Fan Shi, Alan D. Bristow, Lian Li, and Cheng Cen*

Cite This: *Nano Lett.* 2021, 21, 8872–8879 Read Online

ACCESS | Metrics & More | Article Recommendations | Supporting Information

ABSTRACT: The downscaling of nonlinear optical devices is significantly hindered by the inherently weak nonlinearity in regular materials. Here, we report a giant third-harmonic generation discovered in epitaxial thin films of V−VI chalcogenide topological insulators. Using a tailored substrate and capping layer, a single reflection from a 13 nm film can produce a nonlinear conversion efficiency of nearly 0.01%, a performance that rivals micron-scale waveguides made from conventional materials or metasurfaces with far more complex structures. Such strong nonlinear optical emission, absent from the topologically trivial member in the same compound family, is found to be generated by the same bulk band characteristics that are responsible for producing the band inversion and the nontrivial topological ordering. This finding reveals the possibility of obtaining superior optical nonlinearity by examining the large pool of newly discovered topological materials with similar band characteristics.

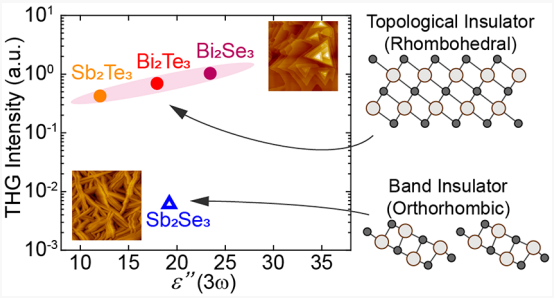

KEYWORDS: *nonlinear optics, topological insulator, heterostructure engineering, molecular beam epitaxy, FDTD simulation, Floquet formalism*

Efficient nonlinear optical (NLO) materials are critical for enabling photon interactions in quantum optics and classical photonic applications.[1−3] The NLO susceptibilities of most materials are very small,[3] with typical values of $\chi^{(2)} \sim 10^{-12}$ m/V and $\chi^{(3)} \sim 10^{-20}$ m^2/V^2. As a result, current NLO devices made of conventional bulk materials typically have large footprints in the mm−cm range and require complicated phase-matching schemes to ensure a sufficient nonlinear conversion efficiency.[4−6] The urgent need to develop chip-scale integrated photonics and compact optical modules that can effectively interface with nanoelectronic devices prompts researchers to actively search for new materials with larger NLO responses.

Recently, large optical nonlinearities have been discovered in various 2D layered compounds.[7,8] With the emergence of topological materials, there are also increasing interests in understanding how band topology affects the NLO properties.[9−13] While many works focus on even-order NLO processes that require broken inversion symmetry,[14−17] here we report a giant third-harmonic generation (THG) in centrosymmetric V−VI topological insulators (TIs).[18] Without any optical resonances,[19−21] broadband third-order susceptibilities ($\chi^{(3)}$) at 10^{-17}−10^{-16} m^2/V^2 level are found. THG output from these films exhibits a strong substrate dependence and an anomalous thickness scaling, revealing important learning experiences for the NLO research in ultrathin 2D materials. We also carried out tight-binding calculations to identify the electronic states that are responsible for the giant THG, explaining the close correlation observed between the THG and the band topology. Since layered TI films can be flexibly integrated with virtually any substrate or capping layer, we show that the already strong THG emissions can be further enhanced by 2 orders of magnitude using tailored heterostructures. These works demonstrate a promising pathway for developing nonlinear nanophotonics using low-dimensional topological materials.

Results. NLO responses of the TI films are studied using pulsed telecom lasers (1560 nm). With a 100 mW incidence (pulse energy density ∼3.2 mJ/cm^2), a THG output of 100 nW is generated by a single reflection at the surface of a 7 QL Bi_2Se_3 film (∼7 nm), a conversion efficiency almost 10^4 times larger than all the benchmark materials tested (Figure 1a). Distinct from materials that only produce strong nonlinear emissions near band structure-related resonances, such as Au,[22] black phosphorus,[20] and graphene,[19] The THG signal detected from TI films is insensitive to the incidence frequency (Figure 1b).

Received: September 1, 2021
Revised: October 2, 2021
Published: October 11, 2021

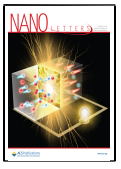

https://doi.org/10.1021/acs.nanolett.1c03376
Nano Lett. 2021, 21, 8872−8879

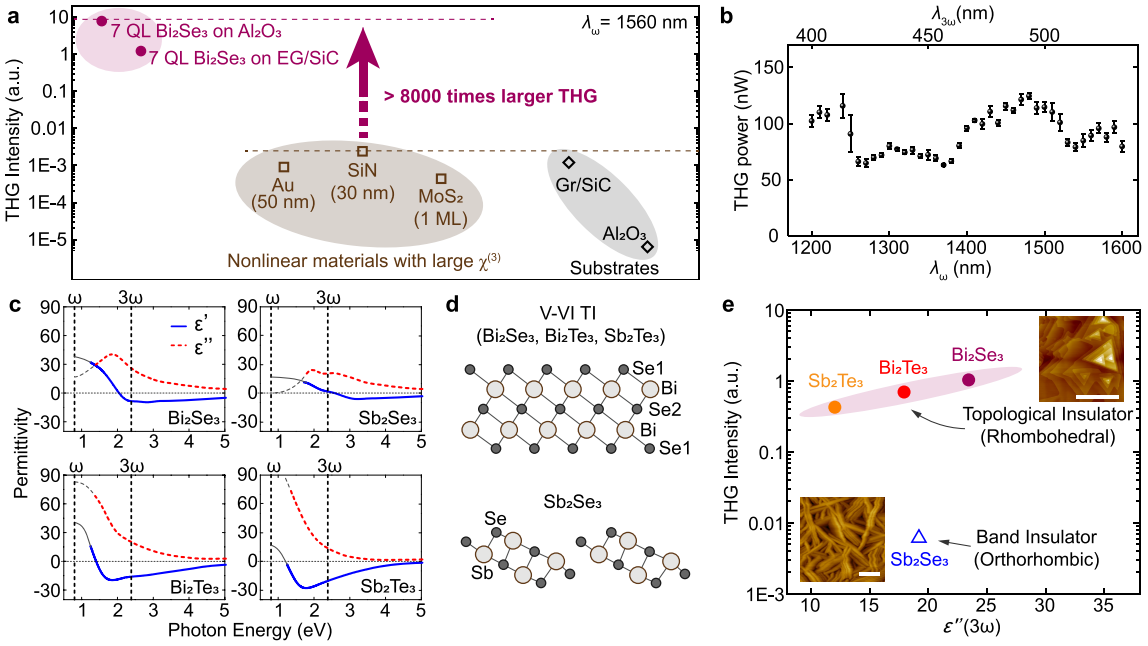

Figure 1. Giant THG in epitaxial TI films. (a) THG from 7 QL Bi_2Se_3 grown on an Al_2O_3 substrate is almost 4 orders of magnitude stronger than well-known NLO materials. (b) THG outputs from 13 QL Bi_2Se_3 films grown on an Al_2O_3 substrate generated by different pump wavelengths. In this experiment, the sample is excited by a 100 mW amplified pulsed laser with 30 GW/cm^2 peak intensity. (c) Complex permittivities of four V−VI chalcogenide films extracted from ellipsometry measurements. (d) Lattice structures of the four V−VI chalcogenides studied in this work. (e) THG intensities of four 10 QL films grown on EG/SiC substrates plotted versus their imaginary permittivity at the THG frequency $\varepsilon''(3\omega)$. Comparing to the three topological insulators, THG intensity found in the band insulator Sb_2Se_3 is much smaller. Insets show the surface topography of Bi_2Se_3 and Sb_2Se_3. Scale bars indicate 500 nm.

Measurements were also performed on three other V−VI chalcogenides: Bi_2Te_3, Sb_2Se_3, and Sb_2Te_3. Among them, Bi_2Te_3 and Sb_2Te_3 are also TIs[18] and iso-structural to Bi_2Se_3, while Sb_2Se_3 is a topologically trivial semiconductor[23] with a different chain-type lattice structure (Figure 1d). As shown in Figure 1c, the linear optical responses of the four compounds are heavily determined by the chalcogen elements. The two selenides have similar complex permittivity spectra that are distinct from those of the two tellurides (Figure 1b). In stark contrast, the THG generated by the four materials follows an entirely different trend: THG emissions from all three TIs are comparably strong (Figure 1e), while the signal from the only regular semiconductor Sb_2Se_3 is 2 orders of magnitude weaker.

Interestingly, the THG generated by TI films is highly sensitive to the substrate material (Figure 2a). Films grown on Al_2O_3 can generate 10× stronger THG emissions than films grown on epitaxial graphene (EG)/SiC. On both substrates, the THG signal drops by more than 2 orders of magnitude when the film thickness (d) increases from 7 QL to 40 QL. We note that, when d is well below the nonlinear coherence length (~200 nm in Bi_2Se_3), many literature works assumed that the nonlinear emission should be proportion to $\chi^{(3)}d^2$.[24−28] Our observations clearly defy such assumption and require a better understanding.

Other than the regular bulk electronic states, the NLO properties of V−VI TIs may also be affected by the Dirac topological surface states (TSSs)[29] and the band-bending induced topologically trivial two-dimensional electron gas (2DEG) states that are localized near the surface and interface.[30] In addition, it is well-known that TIs exposed to the air are subject to surface oxidation.[31] Direct characterizations of these effects are needed before the THG characteristics observed can be fully interpreted. To accomplish this task, in situ angle-resolved photoemission spectroscopy (ARPES) and ex situ terahertz time-domain spectroscopy (THz-TDS) measurements were performed on films of various thicknesses (Figure 2b,c). It can be seen from the ARPES data that the samples in an ultrahigh vacuum are n-type doped and has a ~0.3 eV downward band bending near the film−substrate interface (Figure 2b). The gapless TSSs can be clearly resolved when d > 5 QL. In thinner films, TSSs at the two surfaces start to couple and lead to a gap opening. THz spectra measured in the atmosphere (Figure 2c) are dominated by a Drude-type carrier behavior and a phonon resonance near 2 THz.[32,33] The phonon peak scales linearly with d (Figure 2e), demonstrating a structural uniformity throughout the film. In contrast, the Drude conductance saturates when d exceeds 10 QL (Figure 2d), likely indicating that the electrical transport is dominated by the surface states.[32,33] The extrapolations of the phonon signal and the zero-frequency conductance both reach zero at 2 QL, which we use as a quantification of surface oxidation layer thickness.

On the basis of these results, we now have the necessary inputs for modeling the THG behavior. First, we analytically evaluate how different optical quantities vary as d changes (Supporting Information). As shown in Figure 2g, due to the large refractive index of Bi_2Se_3 and its mismatch with the substrate ($n_{Bi_2Se_3}(\omega) = 7.2 + 1.2i$, $n_{Al_2O_3}(\omega) = 1.7$), the fundamental field strength E_ω decreases as the film becomes thicker. In ultrathin films, the weak surface reflectance, largely determined by the substrate, allows more light into the film and thus produces a larger E_ω. At a larger d, the reflectance increases due to the more significant contribution from Bi_2Se_3, leading to a suppressed E_ω. The variation of E_ω critically impacts THG because of the hexic scaling of the third-order NLO process ($I_{3\omega} \sim (E_\omega)^6$). This effect also explains the

https://doi.org/10.1021/acs.nanolett.1c03376
Nano Lett. 2021, 21, 8872−8879

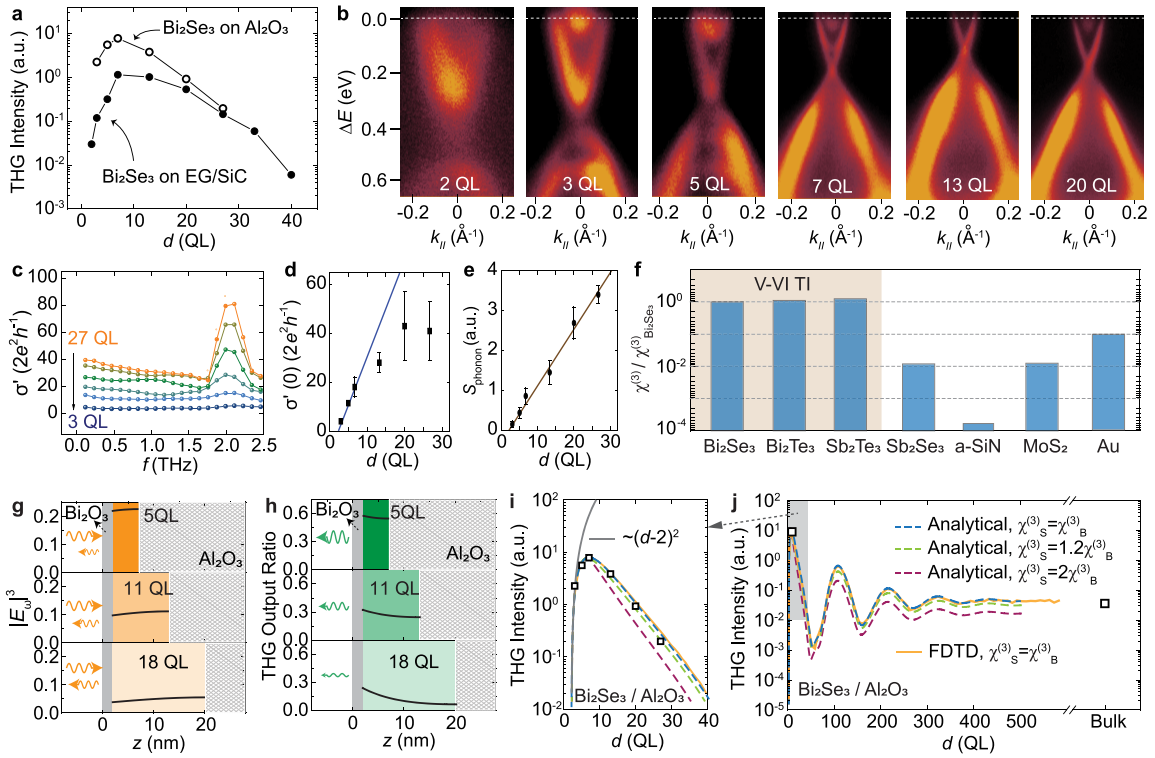

Figure 2. Anomalous thickness dependence of THG. (a) Film thickness dependence of the THG intensity in Bi_2Se_3 films. (b) In situ ARPES spectra of Bi_2Se_3 films with different thicknesses. (c) Terahertz conductance of Bi_2Se_3 films. (d) The extracted zero-frequency Drude conductance plotted versus the film thickness. Error bars represent data variances when the measurement was repeated at different sample positions. (e) Phonon peak area at around 2 THz plotted versus the film thickness. (f) Relative $\chi^{(3)}$ (normalized by the Bi_2Se_3 value) of different materials obtained by processing the experimental data using the FDTD method. (g) Fundamental light field distribution inside the Bi_2Se_3 film for three different film thicknesses. The field strength is normalized by the incidence value. (h) The percentage of THG light generated at different depths inside the Bi_2Se_3 film that can be detected from the top sample surface. (i, j) FDTD and analytical models of the thickness-dependent THG intensity considering three different $\chi^{(3)}$ spatial distributions: a constant $\chi^{(3)}$ throughout the film (blue dashed lines, orange solid lines); $\chi^{(3)}$ in the surface and interface layers is 1.2 times larger than the bulk value (green dashed lines), and $\chi^{(3)}$ in the surface and interface layers is 2 times larger than the bulk (purple dashed lines). Experimental data are plotted in black square dots.

substrate dependence observed. Since the refractive index of SiC (n_{SiC} (ω) = 2.6) is larger than Al_2O_3, the stronger reflectance leads to a weaker THG emission. Another factor to consider is how much THG light generated inside the film can be detected from the surface (Figure 2h), which also decreases in thicker films, further contributing to the quick drop of the THG signal observed between 7 QL and 40 QL.

Once the fundamental field strength and the THG output ratio inside the film are mapped out, the overall THG signal can be calculated for any given $\chi^{(3)}$ distribution. For example, near the surface and the interface, surface states may introduce a local variation of $\chi^{(3)}$. Figure 2i,j compares how the d-dependence of THG is expected to change at different surface to bulk $\chi^{(3)}$ ratios. Below 40 QL, when this ratio is larger, the THG signal drops quicker as a function of d. The experimental data is most consistent with the curves calculated, assuming similar $\chi^{(3)}$ values in the bulk and surface layers (Figure 2i). While $\chi^{(3)}$ near the surface might be slightly larger than in the bulk, the difference should be less than 50%. When d increases further, the THG intensity oscillates with a period around 100 nm ($\sim \lambda_\omega/2n_{Bi_2Se_3}$ (ω)) (Figure 2j). The initially huge oscillation amplitude is gradually damped due to the finite optical penetration depth. When d exceeds 500 nm, the THG intensity converges toward a constant that is ~500 times smaller than the output from a 7 QL film, which is highly consistent with what is measured in commercial Bi_2Se_3 bulk samples.

As shown in Figure 2i, the d-dependence of THG strongly deviates from the quadratic curve ($\chi^{(3)}d^2$) even when d is only a few QLs, forbidding the calibration of $\chi^{(3)}$ using such oversimplified relation. Instead, we use the more rigorous finite-difference time-domain method (FDTD) calculations to extract the $\chi^{(3)}$ values from all four V−VI layered chacogenides using a 30 nm amorphous silicone nitride (a-SiN) membrane as the reference (Supporting Information). Such a reference sample is chosen due to its simple geometry, chemical stability, and lack of optical resonances in relevant frequency ranges. $\chi^{(3)}$ of Bi_2Se_3 is found to be 2737 times larger than a-SiN (Figure 2f). Using the reported value[34] $\chi^{(3)}_{a\text{-}SiN} = 1.9 \times 10^{-20}$ m^2/V^2, $\chi^{(3)}_{Bi_2Se_3}$ can be estimated to be 5.2×10^{-17} m^2/V^2. $\chi^{(3)}$ of the other two TIs are 2−3 times larger: $\chi^{(3)}_{Bi_2Te_3}$ 1.3×10^{-16} m^2/V^2, $\chi^{(3)}_{Sb_2Te_3}$ 1.5×10^{-16} m^2/V^2. In contrast, $\chi^{(3)}$ of the regular semiconductor Sb_2Se_3 is much smaller: $\chi^{(3)}_{Sb_2Se_3}$ 1.4×10^{-18} m^2/V^2.

Next, we explore the electronic origin of the giant $\chi^{(3)}$ found in V−VI TIs using a tight-binding approach that captures the key features of the relevant energy spectrum but, unlike ab initio techniques, does not involve a prohibitively expensive computational cost when modeling quasi 2D structures (i.e., thin films). The energy spectra corresponding to a 15 QL film,

https://doi.org/10.1021/acs.nanolett.1c03376
Nano Lett. 2021, 21, 8872−8879

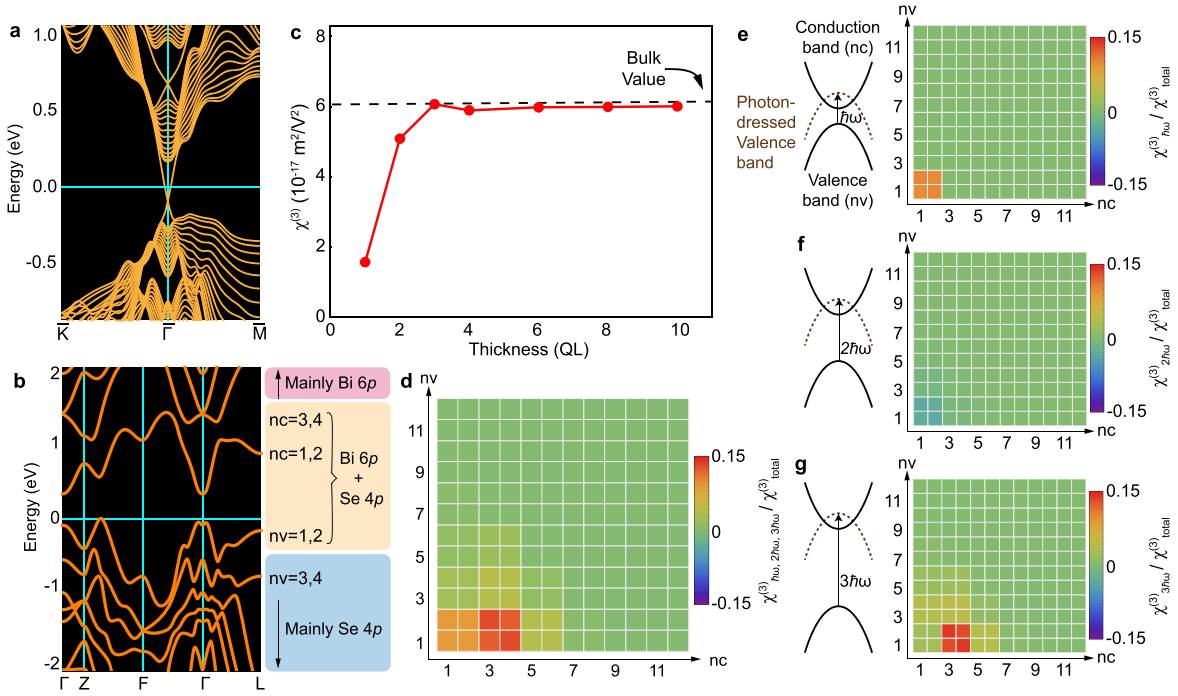

Figure 3. Electronic bands responsible for the giant THG. (a) Band structure of a 15 QL thick Bi_2Se_3 slab. (b) Band structure of bulk Bi_2Se_3. Conduction bands and valence bands are indexed by two integer numbers (*nc* and *nv*) based on their energies. (c) Red dots plot the spatially averaged third-order NLO susceptibilities $\overline{\chi}^{(3)}$ calculated from slab models. The black dashed line indicates the $\overline{\chi}^{(3)}$ value obtained from the bulk model. (d) Band-specific contributions to $\overline{\chi}^{(3)}$ summing all three Floquet processes. (e–g) Relative contributions from specific (*nc*, *nv*) band pairs to $\overline{\chi}^{(3)}$ through each Floquet process.

obtained based on a slab-geometry calculation, and a bulk system, calculated using a 3D geometry, are shown in Figure 3a,b, respectively.

Considering the experimentally obtained doping level and band bending, the NLO properties are calculated using the Keldysh Green's function method in combination with the Floquet formalism (Supporting Information).[9,35−37] Figure 3c shows the spatially averaged thrid-order NLO susceptibility $\overline{\chi}^{(3)}$ calculated for thin films of different thicknesses (red dots) and for a bulk system (black dashed line). Large $\overline{\chi}^{(3)}$ values near 6×10^{-17} m^2/V^2 are found, highly consistent with the value extracted from experimental data. Comparing films with different thicknesses, $\overline{\chi}^{(3)}$ rises first as the thickness increases from 1 QL to 3 QL and then converges to the bulk value. The almost constant $\overline{\chi}^{(3)}$ values found in thicker films suggest that the bulk states are likely the main contributors. When the film thickness drops below 3 QL, the number of confinement-induced subbands approaches zero, leading to a significant reduction in$\overline{\chi}^{(3)}$. The attribution of the large $\overline{\chi}^{(3)}$ to bulk states raises the questions of why is the THG effect particularly strong in V−VI TIs (Bi_2Se_3, Bi_2Te_3, Sb_2Te_3) and what distinguishes the topologically trivial Sb_2Se_3 from them?

To answer the first question, we consider the bulk model, which has far fewer states (20 double degenerate energy bands) and thus allows us to more easily map out the THG contributions from individual conduction-valence band pairs through different Floquet processes (Figure 3e–g). In Figure 3b, conduction and valence bands are indexed by two integer numbers (*nc* and *nv*) based on their energies relative to the Fermi level. It can be seen that $\overline{\chi}^{(3)}$ in Bi_2Se_3 is dominantly generated by the $\hbar\omega$ and $3\hbar\omega$ Floquet processes (Figure 3e,g). THG via the $\hbar\omega$ process is almost entirely produced by the interaction between the top valence band (*nv* = 1, 2) and the bottom conduction band (*nc* = 1, 2), and THG via the $3\hbar\omega$ Floquet process (Figure 3g) is produced by the coupling between *nv* = 1, 2 valence band and *nc* = 3, 4 conduction band. That is to say, while there are many bands involved in the THG process due to the large energy span $\sim 3\hbar\omega$ = 2.4 eV, only the top valence band and the two bottom conduction bands are responsible for the large $\overline{\chi}^{(3)}$.

These low-energy bands are also the ones that generate the nontrivial topological properties in V−VI TIs. In Bi_2Se_3, the coupling between the alternating planes of Bi and Se (Figure 1d) causes the Bi 6p orbitals to strongly hybridize with Se 4p orbitals. The covalent bonding between neighboring Bi−Se atoms dominates the conduction and valence band states near the Fermi level. Without spin−orbit coupling, the *nv* = 1, 2 states are formed from antisymmetric Bi−Se p_z bonding orbitals, and the *nc* = 1, 2, 3, 4 states are formed from the symmetric Bi−Se antibonding orbitals. Under the influence of spin−orbit coupling, in-plane orbitals are strongly mixed with the out-of-plane p_z orbitals, and the *nv* = 1, 2 and *nc* = 1, 2 bands with opposite parities are inverted at the Γ point,[38] leading to the nontrivial topological order, which is not only critical for the formation of the nontrivial band topology but also such band characteristics are also important enablers for a large $\chi^{(3)}$. First, the opposite parities allow the *k*-space integral of the third-order nonlinear current related velocity matrix elements to be nonzero. Second, the similar atomic orbital origin of the *nv*, *nc* states allows maximized wave function overlapping. And third, the spin−orbit coupling effectively mixes the p_x and p_y orbitals into the states near the Fermi level, allowing them to more strongly couple to the in-plane polarized light. Similar band structures are also present in Bi_2Te_3 and Sb_2Te_3, both exhibiting comparably strong THG performances. In contrast, the lattice of Sb_2Se_3 is composed of

https://doi.org/10.1021/acs.nanolett.1c03376
Nano Lett. 2021, 21, 8872−8879

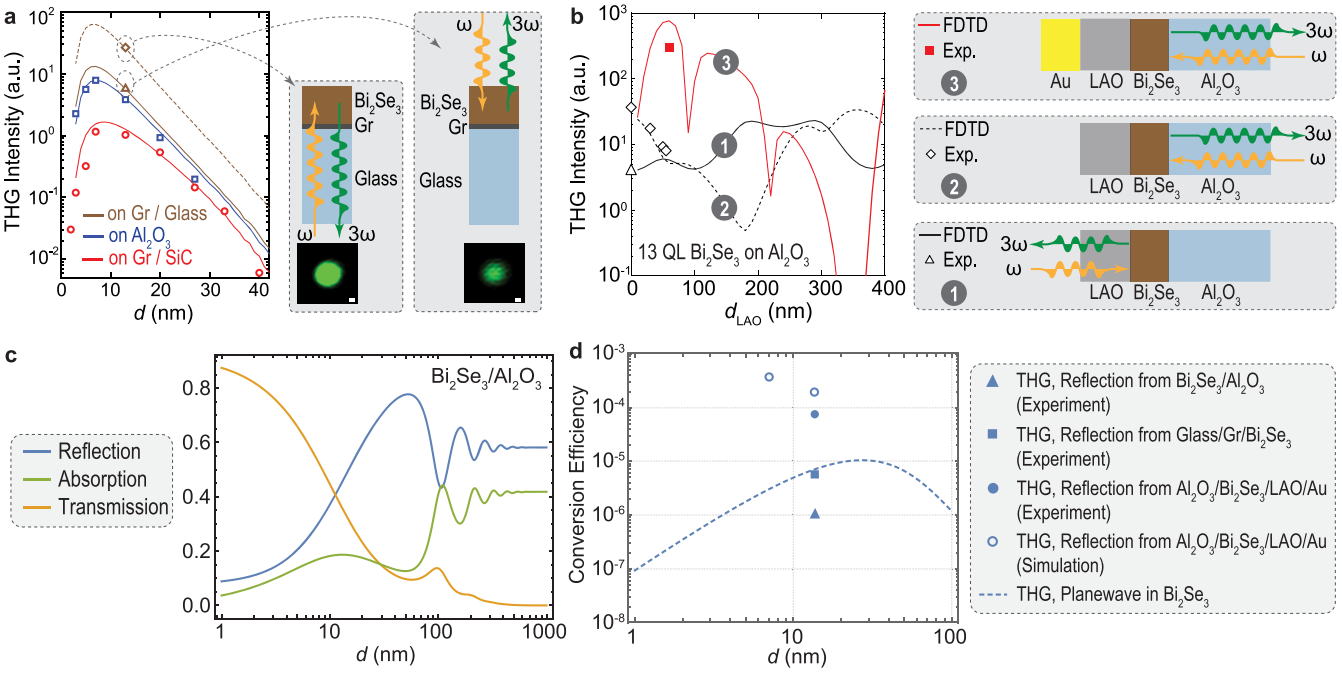

Figure 4. THG enhancement through substrate and capping layer engineering. (a) Experimental data (scattered dots) and FDTD results (solid lines) comparing the THG intensities obtained in Bi_2Se_3 films grown on different substrates (Al_2O_3, EG/SiC, transferred graphene/glass slide). For the same 13 QL film grown on the graphene/glass slide substrate, measurements performed with the fundamental light incident from the film side and the substrate side yield drastically different THG intensities. The inset microscopy images compare the reflected THG emission patterns measured using the two incidence geometries. Scale bars indicate 1 μm. (b) Experimental data (scattered dots) and FDTD results (solid and dashed curves) of the THG emission detected in three different geometries as illustrated. By coating the TI film with amorphous $LaAlO_3$ and Au and detecting from the Al_2O_3 substrate side (Figure 3), a THG enhancement approaching 100 times can be generated. (c) Surface reflectance of the fundamental light, absorptance by the TI film, and transmittance into the substrate plotted versus the film thickness. (d) THG conversion efficiencies that can be achieved by different film stacks. Experimental data were obtained using an amplified femtosecond laser with a peak intensity of 30 GW/cm^2. As a reference, the dashed line plots the calculated results considering a planewave propagating in continuous media.

decoupled 1D chains (Figure 1d), causing the top valence band to be dominated by antibonding states formed from Se p orbitals,[39] leading to a distinct band topology and a greatly reduced $\chi^{(3)}$.

We then discuss how to further enhance the THG conversion efficiency. A common strategy would be to increase the length of the nonlinear medium. However, due to the strong reflection and absorption (Figure 4c), this approach is not feasible in Bi_2Se_3. It can be shown[3] that, in a greatly simplified setup where a planewave is traveling in a continuous medium of Bi_2Se_3, the THG conversion no longer increases once d exceeds 30 nm (Figure 4d).

Alternatively, we seek to enhance THG through substrate and capping layer engineering. A simple demonstration is shown in Figure 4a. A 13 QL Bi_2Se_3 film is grown on a monolayer graphene sheet mechanically transferred on a glass slide. When the incidence and detection are carried out from the substrate side, the glass layer ($n_{glass}(\omega) = 1.5$) between air and Bi_2Se_3 reduces the spatial gradient of $n(\omega)$, allowing more fundamental light into the film. As a result, the THG output is enhanced 8 times, compared to the maximum value observed in Bi_2Se_3/Al_2O_3.

More significant enhancement can be achieved using the film stacks illustrated in Figure 4b. Starting from a 13 QL Bi_2Se_3 film grown on Al_2O_3, amorphous $LaAlO_3$ (LAO) and Au are sequentially deposited on top. By tuning the LAO layer thickness, E_ω inside the TI film and the THG out-coupling ratio can be effectively tuned, producing an orders-of-magnitude larger THG conversion efficiency. To accurately control the LAO layer thickness, the deposition is performed in incremental steps. After each step, the THG intensity is experimentally checked (diamond dots) and compared to the simulation result (black dashed line). Once the consistency between the two sets of data is confirmed, and the optimized thickness (60 nm) is reached, the top Au layer is deposited. The THG output from the final sample (red square dot) is 75 times stronger than the as-grown film, while our simulation predicts an enhancement twice as large (red solid curve). Such difference is likely caused by the nonideal surface quality of the Au film, which is known to produce degraded optical responses as compared to the bulk.[40,41] Figure 4d summarizes the THG conversion efficiencies obtained using different substrate/capping layer designs. Using a simple film stack with an only 13 nm thick NLO medium, an efficiency of nearly 0.01% is achieved in a single reflection, rivaling the performance of nonlinear metasurface structures[42−45] that involve far more complex device fabrications. Once the Au film quality can be improved, it is possible that the single-reflection conversion efficiency can be pushed toward 0.1%.

In conclusion, we have discovered a giant THG in epitaxial V−VI chalcogenide TI films, which exhibit 10^{-17}−10^{-16} m^2/V^2 level $\chi^{(3)}$ in a broad frequency range. In comparison, $\chi^{(3)}$ of the topologically trivial member (Sb_2Se_3) in the same compound family is 2 orders of magnitude smaller, indicating an interesting correlation between the THG efficiency and the band topology. We found that the strong THG is not directly produced by specific topological quantities or the Dirac surface states. Instead, the large $\chi^{(3)}$ is a product of the same bulk band

https://doi.org/10.1021/acs.nanolett.1c03376
Nano Lett. 2021, 21, 8872−8879

characteristics that enable the band inversion and the nontrivial topological ordering in 3D TIs. While topological quantities such as Berry curvature and Berry connection are most prominent in generating NLO effects in THz and mid-infrared frequencies,[15,17,46−48] our studies demonstrate that the related bulk band characteristics in topological materials offer another venue for producing strong NLO responses in the near-infrared to visible frequency window.

The NLO susceptibility of 2D materials reported in the literature is often highly controversial,[8] showing discrepancies up to several orders of magnitude. In this work, we showed that the NLO emissions generated by thin films are highly sensitive to small variations in the heterostructure dimensions and the substrate choices. Therefore, researchers should be very cautious in applying the rudimentary relation of $I_{n\omega} \sim \chi^{(n)} d^2$ when calibrating $\chi^{(n)}$, especially when treating ultrathin 2D materials. Instead, systematic modeling and measurements covering an adequately large parameter space are needed.

We also explored the tuning of the THG output through substrate/capping layer engineering. A single-reflection THG conversion efficiency of around 0.01% was achieved experimentally on a 13 QL Bi_2Se_3 film capped by LAO and Au. Layered TIs have the unique advantage that their thin films can be readily grown by van der Waals epitaxy or mechanically transferred onto almost any substrates without precise lattice matching, allowing them to be flexibly integrated with many existing designs of metasurface structures. Via such integrations, the THG conversion efficiency of TI-based structures can be further enhanced, producing a tantalizing venue for the development of novel flat optics[7,49−52] and nano-optical devices.[53,54]

■ ASSOCIATED CONTENT

Supporting Information

The Supporting Information is available free of charge at https://pubs.acs.org/doi/10.1021/acs.nanolett.1c03376.

Multiphoton microscopy setup; the dependences of the THG signal on the polarization and power of the incident light; methods used for tight-binding model, nonlinear susceptibility calculation, FDTD model, analytical raytracing model, sample synthesis, nonlinear optical measurements, ellipsometry, THz spectrometry, graphene transfer, and interband THG current formula (PDF)

■ AUTHOR INFORMATION

Corresponding Author

Cheng Cen − *Department of Physics and Astronomy, West Virginia University, Morgantown, West Virginia 26506, United States;* orcid.org/0000-0001-8217-0289; Email: chcen@mail.wvu.edu

Authors

Yinxiao Xiang − *Department of Physics and Astronomy, West Virginia University, Morgantown, West Virginia 26506, United States*

Chenhui Yan − *Department of Physics and Astronomy, West Virginia University, Morgantown, West Virginia 26506, United States;* orcid.org/0000-0002-5440-9536

Tudor D. Stanescu − *Department of Physics and Astronomy, West Virginia University, Morgantown, West Virginia 26506, United States*

Yanjun Ma − *Department of Physics and Astronomy, West Virginia University, Morgantown, West Virginia 26506, United States; Process Equipment Division, Kurt J. Lesker Company, Jefferson Hills, Pennsylvania 15025, United States*

Rishmali Sooriyagoda − *Department of Physics and Astronomy, West Virginia University, Morgantown, West Virginia 26506, United States*

Fan Shi − *Department of Physics and Astronomy, West Virginia University, Morgantown, West Virginia 26506, United States; Key Laboratory of Computer Vision and System of Ministry of Education, Tianjin University of Technology, Tianjin 300384, China*

Alan D. Bristow − *Department of Physics and Astronomy, West Virginia University, Morgantown, West Virginia 26506, United States*

Lian Li − *Department of Physics and Astronomy, West Virginia University, Morgantown, West Virginia 26506, United States*

Complete contact information is available at: https://pubs.acs.org/10.1021/acs.nanolett.1c03376

Author Contributions

Y.X. and C.Y. contributed equally. Y.X., R.S., A.B., and C.C. performed the nonlinear optical and AFM measurements. C.Y. and L.L. performed the MBE growth, STM measurements, and ARPES measurements. T.S. carried out the tight-binding modeling and the related nonlinear susceptibility calculation. F.S. performed the THz spectroscopy measurements. Y.M. performed the capping layer growth. C.C. conceived and organized the study. Y.X. and C.C. analyzed the data and wrote the paper. All authors discussed the results and commented on the manuscript.

Notes

The authors declare no competing financial interest.

■ ACKNOWLEDGMENTS

Work performed by C.C.'s group is supported by the Department of Energy (DE-SC-0010399) and the National Science Foundation (NSF 1454950). Work performed by L.L.'s group is supported by the Department of Energy (DE-SC0017632) and the National Science Foundation (EFRI-1741673). Work performed by T.S.'s group is supported by the National Science Foundation (DMR-1414683).

■ REFERENCES

(1) Mandel, L.; Wolf, E. *Optical coherence and quantum optics*; Cambridge university press: Cambridge, 1995.

(2) Chang, D. E.; Vuletić, V.; Lukin, M. D. Quantum nonlinear optics — photon by photon. *Nat. Photonics* **2014**, *8* (9), 685−694.

(3) Boyd, R. W. *Nonlinear optics*; Elsevier: London, 2003.

(4) Billat, A.; Grassani, D.; Pfeiffer, M. H. P.; Kharitonov, S.; Kippenberg, T. J.; Brès, C.-S. Large second harmonic generation enhancement in Si3N4 waveguides by all-optically induced quasi-phase-matching. *Nat. Commun.* **2017**, *8* (1), 1016.

(5) Lin, J.; Bo, F.; Cheng, Y.; Xu, J. Advances in on-chip photonic devices based on lithium niobate on insulator. *Photonics Res.* **2020**, *8* (12), 1910−1936.

(6) Timurdogan, E.; Poulton, C. V.; Byrd, M. J.; Watts, M. R. Electric field-induced second-order nonlinear optical effects in silicon waveguides. *Nat. Photonics* **2017**, *11* (3), 200−206.

(7) You, J. W.; Bongu, S. R.; Bao, Q.; Panoiu, N. C. Nonlinear optical properties and applications of 2D materials: theoretical and experimental aspects. *Nanophotonics* **2018**, *8* (1), 63−97.

(8) Autere, A.; Jussila, H.; Dai, Y.; Wang, Y.; Lipsanen, H.; Sun, Z. Nonlinear Optics with 2D Layered Materials. *Adv. Mater.* **2018**, *30* (24), 1705963.
(9) Morimoto, T.; Nagaosa, N. Topological nature of nonlinear optical effects in solids. *Science Advances* **2016**, *2* (5), e1501524.
(10) Cook, A. M.; M. Fregoso, B.; de Juan, F.; Coh, S.; Moore, J. E. Design principles for shift current photovoltaics. *Nat. Commun.* **2017**, *8*, 14176.
(11) Luu, T. T.; Wörner, H. J. Measurement of the Berry curvature of solids using high-harmonic spectroscopy. *Nat. Commun.* **2018**, *9* (1), 916.
(12) Parker, D. E.; Morimoto, T.; Orenstein, J.; Moore, J. E. Diagrammatic approach to nonlinear optical response with application to Weyl semimetals. *Phys. Rev. B: Condens. Matter Mater. Phys.* **2019**, *99* (4), 045121.
(13) Ma, J.; Gu, Q.; Liu, Y.; Lai, J.; Yu, P.; Zhuo, X.; Liu, Z.; Chen, J.-H.; Feng, J.; Sun, D. Nonlinear photoresponse of type-II Weyl semimetals. *Nat. Mater.* **2019**, *18* (5), 476−481.
(14) Wu, L.; Patankar, S.; Morimoto, T.; Nair, N. L.; Thewalt, E.; Little, A.; Analytis, J. G.; Moore, J. E.; Orenstein, J. Giant anisotropic nonlinear optical response in transition metal monopnictide Weyl semimetals. *Nat. Phys.* **2017**, *13*, 350.
(15) Osterhoudt, G. B.; Diebel, L. K.; Gray, M. J.; Yang, X.; Stanco, J.; Huang, X.; Shen, B.; Ni, N.; Moll, P. J. W.; Ran, Y.; Burch, K. S. Colossal mid-infrared bulk photovoltaic effect in a type-I Weyl semimetal. *Nat. Mater.* **2019**, *18* (5), 471−475.
(16) Rees, D.; Manna, K.; Lu, B.; Morimoto, T.; Borrmann, H.; Felser, C.; Moore, J. E.; Torchinsky, D. H.; Orenstein, J. Helicity-dependent photocurrents in the chiral Weyl semimetal RhSi. *Science Advances* **2020**, *6* (29), eaba0509.
(17) Ni, Z.; Wang, K.; Zhang, Y.; Pozo, O.; Xu, B.; Han, X.; Manna, K.; Paglione, J.; Felser, C.; Grushin, A. G.; de Juan, F.; Mele, E. J.; Wu, L. Giant topological longitudinal circular photo-galvanic effect in the chiral multifold semimetal CoSi. *Nat. Commun.* **2021**, *12* (1), 154.
(18) Zhang, H.; Liu, C.-X.; Qi, X.-L.; Dai, X.; Fang, Z.; Zhang, S.-C. Topological insulators in Bi_2Se_3, Bi_2Te_3 and Sb_2Te_3 with a single Dirac cone on the surface. *Nat. Phys.* **2009**, *5*, 438.
(19) Jiang, T.; Huang, D.; Cheng, J.; Fan, X.; Zhang, Z.; Shan, Y.; Yi, Y.; Dai, Y.; Shi, L.; Liu, K.; Zeng, C.; Zi, J.; Sipe, J. E.; Shen, Y.-R.; Liu, W.-T.; Wu, S. Gate-tunable third-order nonlinear optical response of massless Dirac fermions in graphene. *Nat. Photonics* **2018**, *12* (7), 430−436.
(20) Rodrigues, M. J. L. F.; de Matos, C. J. S.; Ho, Y. W.; Peixoto, H.; de Oliveira, R. E. P.; Wu, H.-Y.; Neto, A. H. C.; Viana-Gomes, J. Resonantly Increased Optical Frequency Conversion in Atomically Thin Black Phosphorus. *Adv. Mater.* **2016**, *28* (48), 10693−10700.
(21) Wang, G.; Marie, X.; Gerber, I.; Amand, T.; Lagarde, D.; Bouet, L.; Vidal, M.; Balocchi, A.; Urbaszek, B. Giant Enhancement of the Optical Second-Harmonic Emission of WSe_2 Monolayers by Laser Excitation at Exciton Resonances. *Phys. Rev. Lett.* **2015**, *114* (9), 097403.
(22) Boyd, R. W.; Shi, Z.; De Leon, I. The third-order nonlinear optical susceptibility of gold. *Opt. Commun.* **2014**, *326*, 74−79.
(23) Zhou, Y.; Wang, L.; Chen, S.; Qin, S.; Liu, X.; Chen, J.; Xue, D.-J.; Luo, M.; Cao, Y.; Cheng, Y.; Sargent, E. H.; Tang, J. Thin-film Sb_2Se_3 photovoltaics with oriented one-dimensional ribbons and benign grain boundaries. *Nat. Photonics* **2015**, *9*, 409.
(24) Karvonen, L.; Säynätjoki, A.; Mehravar, S.; Rodriguez, R. D.; Hartmann, S.; Zahn, D. R. T.; Honkanen, S.; Norwood, R. A.; Peyghambarian, N.; Kieu, K.; Lipsanen, H.; Riikonen, J. Investigation of Second- and Third-Harmonic Generation in Few-Layer Gallium Selenide by Multiphoton Microscopy. *Sci. Rep.* **2015**, *5* (1), 10334.
(25) Susoma, J.; Karvonen, L.; Säynätjoki, A.; Mehravar, S.; Norwood, R. A.; Peyghambarian, N.; Kieu, K.; Lipsanen, H.; Riikonen, J. Second and third harmonic generation in few-layer gallium telluride characterized by multiphoton microscopy. *Appl. Phys. Lett.* **2016**, *108* (7), 073103.
(26) Kumar, N.; Kumar, J.; Gerstenkorn, C.; Wang, R.; Chiu, H.-Y.; Smirl, A. L.; Zhao, H. Third harmonic generation in graphene and few-layer graphite films. *Phys. Rev. B: Condens. Matter Mater. Phys.* **2013**, *87* (12), 121406.
(27) Säynätjoki, A.; Karvonen, L.; Riikonen, J.; Kim, W.; Mehravar, S.; Norwood, R. A.; Peyghambarian, N.; Lipsanen, H.; Kieu, K. Rapid Large-Area Multiphoton Microscopy for Characterization of Graphene. *ACS Nano* **2013**, *7* (10), 8441−8446.
(28) Karvonen, L.; Säynätjoki, A.; Huttunen, M. J.; Autere, A.; Amirsolaimani, B.; Li, S.; Norwood, R. A.; Peyghambarian, N.; Lipsanen, H.; Eda, G.; Kieu, K.; Sun, Z. Rapid visualization of grain boundaries in monolayer MoS2 by multiphoton microscopy. *Nat. Commun.* **2017**, *8* (1), 15714.
(29) Zhang, Y.; He, K.; Chang, C.-Z.; Song, C.-L.; Wang, L.-L.; Chen, X.; Jia, J.-F.; Fang, Z.; Dai, X.; Shan, W.-Y.; Shen, S.-Q.; Niu, Q.; Qi, X.-L.; Zhang, S.-C.; Ma, X.-C.; Xue, Q.-K. Crossover of the three-dimensional topological insulator Bi_2Se_3 to the two-dimensional limit. *Nat. Phys.* **2010**, *6*, 584.
(30) Bianchi, M.; Guan, D.; Bao, S.; Mi, J.; Iversen, B. B.; King, P. D. C.; Hofmann, P. Coexistence of the topological state and a two-dimensional electron gas on the surface of Bi_2Se_3. *Nat. Commun.* **2010**, *1* (1), 128.
(31) Kong, D.; Cha, J. J.; Lai, K.; Peng, H.; Analytis, J. G.; Meister, S.; Chen, Y.; Zhang, H.-J.; Fisher, I. R.; Shen, Z.-X.; Cui, Y. Rapid Surface Oxidation as a Source of Surface Degradation Factor for Bi_2Se_3. *ACS Nano* **2011**, *5* (6), 4698−4703.
(32) Park, B. C.; Kim, T.-H.; Sim, K. I.; Kang, B.; Kim, J. W.; Cho, B.; Jeong, K.-H.; Cho, M.-H.; Kim, J. H. Terahertz single conductance quantum and topological phase transitions in topological insulator Bi_2Se_3 ultrathin films. *Nat. Commun.* **2015**, *6*, 6552.
(33) Valdés Aguilar, R.; Stier, A. V.; Liu, W.; Bilbro, L. S.; George, D. K.; Bansal, N.; Wu, L.; Cerne, J.; Markelz, A. G.; Oh, S.; Armitage, N. P. Terahertz Response and Colossal Kerr Rotation from the Surface States of the Topological Insulator Bi_2Se_3. *Phys. Rev. Lett.* **2012**, *108* (8), 087403.
(34) Ning, T.; Hyvärinen, O.; Pietarinen, H.; Kaplas, T.; Kauranen, M.; Genty, G. Third-harmonic UV generation in silicon nitride nanostructures. *Opt. Express* **2013**, *21* (2), 2012−2017.
(35) Jauho, A.-P.; Wingreen, N. S.; Meir, Y. Time-dependent transport in interacting and noninteracting resonant-tunneling systems. *Phys. Rev. B: Condens. Matter Mater. Phys.* **1994**, *50* (8), 5528−5544.
(36) Johnsen, K.; Jauho, A.-P. Quasienergy Spectroscopy of Excitons. *Phys. Rev. Lett.* **1999**, *83* (6), 1207−1210.
(37) Kohler, S.; Lehmann, J.; Hänggi, P. Driven quantum transport on the nanoscale. *Phys. Rep.* **2005**, *406* (6), 379−443.
(38) Liu, C.-X.; Qi, X.-L.; Zhang, H.; Dai, X.; Fang, Z.; Zhang, S.-C. Model Hamiltonian for topological insulators. *Phys. Rev. B: Condens. Matter Mater. Phys.* **2010**, *82* (4), 045122.
(39) Li, Y.; Sun, Y.; Na, G.; Saidi, W. A.; Zhang, L. Diverse electronic properties of 2D layered Se-containing materials composed of quasi-1D atomic chains. *Phys. Chem. Chem. Phys.* **2020**, *22* (4), 2122−2129.
(40) Pandey, S.; Gupta, B.; Chanana, A.; Nahata, A. Non-Drude like behaviour of metals in the terahertz spectral range. *Advances in Physics: X* **2016**, *1* (2), 176−193.
(41) Liang, Y.; Pakniyat, S.; Xiang, Y.; Chen, J.; Shi, F.; Hanson, G. W.; Cen, C. Tunable unidirectional surface plasmon polaritons at the interface between gyrotropic and isotropic conductors. *Optica* **2021**, *8* (7), 952−959.
(42) Shcherbakov, M. R.; Neshev, D. N.; Hopkins, B.; Shorokhov, A. S.; Staude, I.; Melik-Gaykazyan, E. V.; Decker, M.; Ezhov, A. A.; Miroshnichenko, A. E.; Brener, I.; Fedyanin, A. A.; Kivshar, Y. S. Enhanced Third-Harmonic Generation in Silicon Nanoparticles Driven by Magnetic Response. *Nano Lett.* **2014**, *14* (11), 6488−6492.
(43) Liu, S.; Sinclair, M. B.; Saravi, S.; Keeler, G. A.; Yang, Y.; Reno, J.; Peake, G. M.; Setzpfandt, F.; Staude, I.; Pertsch, T.; Brener, I. Resonantly Enhanced Second-Harmonic Generation Using III−V Semiconductor All-Dielectric Metasurfaces. *Nano Lett.* **2016**, *16* (9), 5426−5432.

https://doi.org/10.1021/acs.nanolett.1c03376
Nano Lett. 2021, 21, 8872−8879

(44) Yang, Y.; Wang, W.; Boulesbaa, A.; Kravchenko, I. I.; Briggs, D. P.; Puretzky, A.; Geohegan, D.; Valentine, J. Nonlinear Fano-Resonant Dielectric Metasurfaces. *Nano Lett.* **2015**, *15* (11), 7388−7393.
(45) Lee, J.; Nookala, N.; Gomez-Diaz, J. S.; Tymchenko, M.; Demmerle, F.; Boehm, G.; Amann, M.-C.; Alù, A.; Belkin, M. A. Ultrathin Second-Harmonic Metasurfaces with Record-High Nonlinear Optical Response. *Adv. Opt. Mater.* **2016**, *4* (5), 664−670.
(46) Ahn, J.; Guo, G.-Y.; Nagaosa, N. Low-Frequency Divergence and Quantum Geometry of the Bulk Photovoltaic Effect in Topological Semimetals. *Phys. Rev. X* **2020**, *10* (4), 041041.
(47) Luo, L.; Cheng, D.; Song, B.; Wang, L.-L.; Vaswani, C.; Lozano, P. M.; Gu, G.; Huang, C.; Kim, R. H. J.; Liu, Z.; Park, J.-M.; Yao, Y.; Ho, K.; Perakis, I. E.; Li, Q.; Wang, J. A light-induced phononic symmetry switch and giant dissipationless topological photocurrent in ZrTe5. *Nat. Mater.* **2021**, *20* (3), 329−334.
(48) Chang, G.; Yin, J.-X.; Neupert, T.; Sanchez, D. S.; Belopolski, I.; Zhang, S. S.; Cochran, T. A.; Chéng, Z.; Hsu, M.-C.; Huang, S.-M.; Lian, B.; Xu, S.-Y.; Lin, H.; Hasan, M. Z. Unconventional Photocurrents from Surface Fermi Arcs in Topological Chiral Semimetals. *Phys. Rev. Lett.* **2020**, *124* (16), 166404.
(49) Capasso, F. The future and promise of flat optics: a personal perspective. *Nanophotonics* **2018**, *7* (6), 953−957.
(50) Krasnok, A.; Tymchenko, M.; Alù, A. Nonlinear metasurfaces: a paradigm shift in nonlinear optics. *Mater. Today* **2018**, *21* (1), 8−21.
(51) Camacho-Morales, R.; Xu, L.; Dimitrov, N.; Stoyanov, L.; Ma, Z.; Dreischuh, A. A.; Tan, H. H. H.; De Angelis, C.; Jagadish, C.; Miroshnichenko, A. E.; Rocco, D.; Gili, V. F.; Komar, A.; Lysevych, M.; Karouta, F.; Leo, G.; Rahmani, M.; Neshev, D. N. Infrared upconversion imaging in nonlinear metasurfaces. *Advanced Photonics* **2021**, *3* (3), No. 036002.
(52) Mesch, M.; Metzger, B.; Hentschel, M.; Giessen, H. Nonlinear Plasmonic Sensing. *Nano Lett.* **2016**, *16* (5), 3155−3159.
(53) Reserbat-Plantey, A.; Epstein, I.; Torre, I.; Costa, A. T.; Gonçalves, P. A. D.; Mortensen, N. A.; Polini, M.; Song, J. C. W.; Peres, N. M. R.; Koppens, F. H. L. Quantum Nanophotonics in Two-Dimensional Materials. *ACS Photonics* **2021**, *8* (1), 85−101.
(54) Xia, F.; Wang, H.; Xiao, D.; Dubey, M.; Ramasubramaniam, A. Two-dimensional material nanophotonics. *Nat. Photonics* **2014**, *8* (12), 899−907.

https://doi.org/10.1021/acs.nanolett.1c03376
Nano Lett. 2021, 21, 8872−8879